

Learning Low-dimensional Manifolds for Scoring of Tissue Microarray Images

Donghui Yan[†], Jian Zou[§], Zhenpeng Li[‡]

[†]Mathematics and Data Science, UMass Dartmouth, MA, USA

[§]Mathematical Sciences, Worcester Polytechnic Institute, MA, USA

[‡]Statistics, Dali University, Yunnan, China

February 24, 2021

Abstract

Tissue microarray (TMA) images have emerged as an important high-throughput tool for cancer study and the validation of biomarkers. Efforts have been dedicated to further improve the accuracy of TACOMA, a cutting-edge automatic scoring algorithm for TMA images. One major advance is due to *deepTacoma*, an algorithm that incorporates suitable deep representations of a group nature. Inspired by the recent advance in semi-supervised learning and deep learning, we propose *mfTacoma* to learn alternative deep representations in the context of TMA image scoring. In particular, *mfTacoma* learns the low-dimensional manifolds, a common latent structure in high dimensional data. Deep representation learning and manifold learning typically requires large data. By encoding deep representation of the manifolds as regularizing features, *mfTacoma* effectively leverages the manifold information that is potentially crude due to small data. Our experiments show that deep features by manifolds outperforms two alternatives—deep features by linear manifolds with principal component analysis or by leveraging the group property.

Index terms— Deep representation learning; small data; manifold learning; tissue microarray images

1 Introduction

Tissue microarray (TMA) images [53, 33, 9] have emerged as an important high-throughput tool for the evaluation of histology-based laboratory tests. They are used extensively in cancer studies [20, 9, 25, 50], including clinical outcome analysis [25], tumor progression analysis [38, 1], the identification of diagnostic or prognostic factors [19, 1] etc. TMA images have also been used in the development and validation of tumor-specific biomarkers [25]. Additionally, they are used in imaging genetics [11, 27] for the study of genetics alterations. TMA images are produced from thin slices of tissue sections cut from small tissue cores (less than 1 mm in diameter) which are extracted from tumor blocks. Many slices, typically several hundred (possibly from different patients), are arranged as an array and mounted on a TMA slide, and then stained with a tumor-specific

biomarker. A TMA image can be produced for each tissue section (i.e., a cell in the TMA slide) when viewed with a high-resolution microscope. Figure 1 is an illustration of the TMA technology.

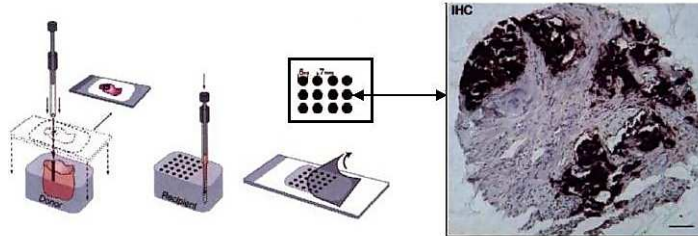


Figure 1: An illustration of the TMA technology (image courtesy [56]). Small tissue cores are first extracted from tumor blocks, and stored in archives. Then thin slices of tissue sections are taken from the tissue core. Hundreds of tissue sections are mounted, in the form of an array, on a tissue slide, and stained with tumor-specific biomarkers. A TMA image is captured for each tissue section when viewed from a high-resolution microscope.

Spots in a TMA image measure tumor-specific protein expression level. The readings of a TMA image are quantified by its staining pattern, which is typically summarized as a numerical score by the pathologist. A protein marker that is highly expressed in tumor cells will exhibit a qualitatively different pattern (e.g., in darker color) from otherwise. Such scores serve as a convenient proxy to study the tissue images. To liberate pathologists from intensive labors, and also to reduce the inherent variability and subjectivity with manual scoring [48, 31, 14, 51, 20, 5, 16, 52, 4, 9] of TMA images, a number of commercial tools and algorithms have been developed. This includes *ACIS*, *Ariol*, *TMAx* and *TMALab II* for IHC, and *AQUA* [8] for fluorescent images. However, these typically require background subtraction, segmentation or landmark selection etc, and are sensitive to factors such as IHC staining quality, background antibody binding, hematoxylin counterstaining, and chromogenic reaction products used to detect antibody binding [56]. The primary difficulty in TMA image analysis is the lack of easily-quantified criteria for scoring—the staining patterns are not localized in position, shape or size.

A major breakthrough was achieved with TACOMA [56], a scoring algorithm that is comparable to pathologists, in terms of accuracy and repeatability, and is robust against variability in image intensity and staining patterns etc. The key insight underlying TACOMA is that, despite significant heterogeneity among TMA images, they exhibit strong statistical regularity in the form of visually observable textures or *staining patterns*. Such patterns are captured by a highly effective image statistics—the gray level co-occurrence matrix (GLCM). Inspired by the success of deep learning [28, 34], *deepTacoma* [55] incorporates deep representations to meet major challenges—heterogeneity and label noise—in the analysis of TMA images. The deep features explored by *deepTacoma* are of a group nature, aiming at giving more concrete information than implied by the labels or to borrow information from “similar” instances, in analogy to how the cluster assumption would help in semi-supervised learning [13, 59].

How to further advance the state-of-the-art? Motivated by progress made with *deepTacoma*, we will further explore deep representations derived from latent structures in the data. While *deepTacoma* makes use of *clusters* in the data, we pursue the low-dimensional manifolds in the present work. For high dimensional data, often the data or part of it lie on some low-dimensional manifolds [47, 43, 17, 26, 12, 6, 41]. Effectively leveraging the manifold information can improve many tasks, such as dimension reduction or model fitting etc. Indeed, a recent work on the geometry of deep learning [35] attributes the success of deep learning to the effectiveness of the deep neural networks in learning such structures in the data. As our method is built upon TACOMA and uses manifold information, we term it *mfTacoma*.

Given the overwhelming popularity of deep learning in image recognition, it is worthwhile to remark the challenges in applying deep learning to TMA images [55]. The availability of large training sample, essential for the success of deep learning, is severely limited for TMA images. TMA images are much harder to acquire than the usual natural images as they have to be taken from the human body and captured by high-end microscopes and imaging devices. Their labelling requires substantial expertise from pathologists. Additionally, the natural and TMA images are of a different nature in terms of classification. Natural images are typically formed by a visually sensible image hierarchy, which leads to the necessary sparsity for deep neural networks to succeed [44]. In contrast, the scoring of TMA images is not about the shape of the staining pattern, rather the “severity and spread” of staining matters. A further limiting fact is that TMA images are scored by biomarkers or cancer types; there are over 100 cancer types according to the US National Cancer Institute [49].

Our main contributions are as follows. First, we propose an effective approach to learn the low dimensional manifolds in high dimensional data, which allows us to advance the state-of-the-art in the scoring of TMA images. The approach is conceptually simple and easy to implement thanks to progress in deep neural networks during the last decades. Second, our approach demonstrates that representing low dimensional manifolds as regularizing features is a fruitful way of leveraging manifold information, effectively overcoming the difficulty that shadows many manifold learning algorithms under small sample. Given the prevalence of low dimensional manifolds in high dimensional data, our approach may be potentially applicable to many problems involving high dimensional data.

The remainder of this paper is organized as follows. We describe the *mfTacoma* algorithm in Section 2. In Section 3, we present our experimental results. Section 4 provides a summary of the methods and results. Given the

2 The *mfTacoma* algorithm

In this section, we will describe the *mfTacoma* algorithm. The scoring systems adopted in practice typically use a small number of discrete values, such as $\{0, 1, 2, 3\}$, as the score (or label) for TMA images. The scoring

criteria are: ‘0’ indicates a definite negative (no staining of tumor cells), ‘3’ a definitive positive (majority cancer cells show dark staining), ‘2’ for positive (small portion of tumor cells show staining or a majority show weak staining), and ‘1’ indicates weak staining in small part of tumor cells, or image in discardable quality [37]. We formulate the scoring of TMA images as a classification problem, following ([56]; [55]).

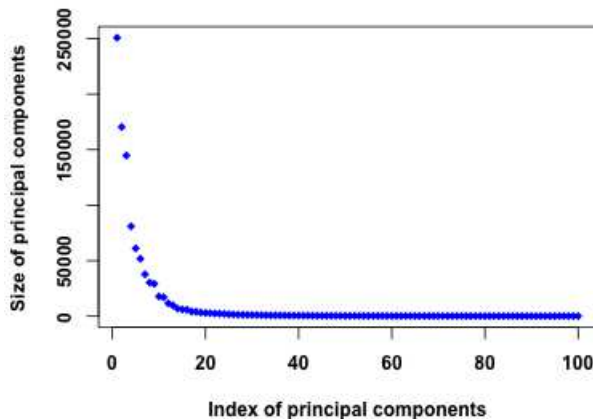


Figure 2: *Size of top 100 principal components of TMA images (in GLCM).*

The representations we explore are derived from the low-dimensional manifold structure in the data. The existence of low-dimensional manifolds in high dimensional data is well established [47, 43, 17, 32, 26, 12, 6]. For TMA images, as the dimension of the ambient space (i.e., the image size) is 1504 x 1440, it is hard to “see” the low-dimensional manifolds. We will instead carry out a principal component analysis (PCA) [30, 45, 58, 46] on the GLCM of all the TMA images to get a crude sense. Figure 2 shows a sharp decay of the principal components and their vanishing beyond the 50th component, and this clearly implies the existence of low-dimensional manifolds. Note that while PCA extracts linear manifolds, the actual manifolds maybe be highly nonlinear. Nevertheless, a simple PCA analysis should be fairly suggestive of their existence. The low-dimensional manifolds are a global property of the data and is beyond what may be revealed by features derived from individual data points alone. Therefore we expect such information help in the scoring of TMA images. One could view the information revealed by manifolds as regularization by problem structures in model fitting. Thus a better model (e.g., more stable or more accurate) would be expected.

One technical challenge is how to extract or make use of the manifold information from the space formed by the TMA images. Manifold learning has been an active research area during the last two decades [32, 12]. Many work deal with dimension reduction or data visualization, for example, Isomap [47], locally linear embedding [43], Laplacian eigenmaps [2], Hessian eigenmaps [17], local tangent space alignment [57], diffusion maps [39], metric manifold maps [41]. Some of these were also used as a data-driven distance metric for image similarity [42]. A more fruitful

line of work seems to be the use of manifolds for regularization in model fitting. This is likely due to the difficulty in estimating the manifolds—the manifolds may be highly nonlinear and the sample size is often disproportionately small, thus using manifolds as auxiliary information may be more productive. Indeed Belkin et al [3] successfully used the graph Laplacian as a regularizer in semi-supervised learning, and Osher and his colleagues [40] use the dimension of the manifold as a regularizer in image denoising.

We follow a similar line as [3, 40] but with representations derived from the low-dimensional manifolds as *regularizing features* to be appended to the input. This is particularly easy to implement, without having to solve a complicated optimization problem, and is fairly general. The effectiveness of using regularizing features has been demonstrated in [55]. Thanks to the availability and easy implementation of autoencoder [22], we will use it to extract the low-dimensional manifold representation corresponding to the TMA images. We term such deep representations as M-features. Figure 3 is an illustration of the feature hierarchy in *mfTacoma*.

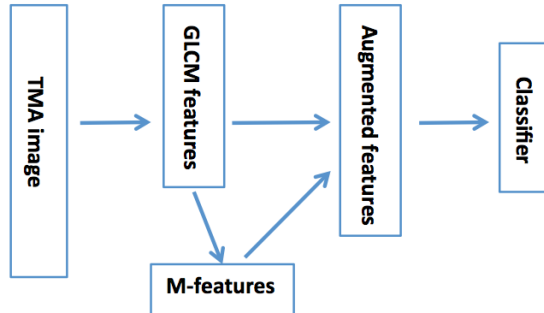


Figure 3: *Illustration of feature hierarchy in mfTacoma.*

The *mfTacoma* algorithm is fairly simple to describe. First, all TMA images are converted to their GLCM representations. Then the GLCMs are input to the autoencoder to extract the deep features, to be concatenated with the GLCMs. The manifold-augmented features and their respective scores are fed to a training algorithm. The trained classifier will be applied to get scores for TMA images in the test set. To give an algorithmic description to *mfTacoma*, assume there are n training instances, m test instances, and $N = n + m$. Denote the training sample by $(I_1, Y_1), \dots, (I_n, Y_n)$ where I_i 's are images and Y_i 's are scores (thus $Y_i \in \{0, 1, 2, 3\}$). Let I_{n+1}, \dots, I_{n+m} be new TMA images that one wish to score (i.e., the test set has a size of m). *mfTacoma* is described as Algorithm 1.

For the rest of this section, we will briefly describe the GLCM and autoencoder.

2.1 The gray level co-occurrence matrix

The GLCM is one of the most widely used image statistics for textured images, such as satellite images and high-resolution tissue images. It

Algorithm 1 The *mfTacoma* algorithm

- 1: for $i = 1$ to N
 - 2: Compute GLCM of image I_i ;
 - 3: Denote the resulting GLCM by X_i ;
 - 4: endfor
 - 5: Find manifold representation $\cup_{i=1}^N \{Z_i\}$ for $\cup_{i=1}^N \{X_i\}$ with an autoencoder;
 - 6: Concatenate X_i and Z_i and get X_i^M , $i = 1, \dots, N$;
 - 7: Feed $\cup_{i=1}^n \{(X_i^M, Y_i)\}$ to RF to obtain a classification rule \hat{f} ;
 - 8: Apply \hat{f} to X_i^M to obtain scores for images I_i for $i = n + 1, \dots, n + m$.
-

can be crudely viewed as a “spatial histogram” of neighboring pixels in an image. It has been successfully applied in a variety of applications [24, 21, 36, 56, 55]. We follow notations used in [56, 54].

The GLCM is defined with respect to a particular spatial relationship of two neighboring pixels. The spatial relationship entails two aspects—a spatial direction, in set $\{\nearrow, \searrow, \nwarrow, \swarrow, \downarrow, \uparrow, \rightarrow, \leftarrow\}$, and the distance between the pair of pixels along the direction. For a given spatial relationship, the GLCM for an image is defined as a $N_g \times N_g$ matrix with its (a, b) -entry being the number of times two pixels with gray values $a, b \in \{1, 2, \dots, N_g\}$ are spatial neighbors; here N_g is the number of gray levels or quantization levels in the image. Note that, for each spatial relationship, one can define a GLCM thus one image can correspond to multiple GLCMs. The definition of GLCM is illustrated in Figure 4 with a toy image (taken from [55]). For a balance of computational efficiency and discriminative power, we take $N_g = 51$ and uniform quantization [23] is applied over the 256 gray levels.

$$\begin{pmatrix} 1 & 2 & 3 & \mathbf{1} \\ 2 & 1 & \mathbf{2} & 3 \\ 1 & \mathbf{1} & 3 & 3 \\ \mathbf{2} & 2 & 1 & 3 \end{pmatrix} \quad \begin{matrix} & \mathbf{1} & \mathbf{2} & \mathbf{3} \\ \mathbf{1} & \begin{pmatrix} 1 & 1 & 2 \end{pmatrix} \\ \mathbf{2} & \begin{pmatrix} 2 & 1 & 1 \end{pmatrix} \\ \mathbf{3} & \begin{pmatrix} 0 & 0 & 1 \end{pmatrix} \end{matrix}$$

Figure 4: **Illustration of GLCM via a toy image** (image taken from [55]). In the 4×4 toy image, there are three gray levels, $\{1, 2, 3\}$; the resulting GLCM for spatial relationship $(\nearrow, 1)$ is a 3×3 matrix.

2.2 Autoencoder with deep networks

An autoencoder is a special type of deep neural network with the inputs and outputs being the same. A neural network is a layered network that tries to emulate the network of connected biological neurons in the human brain; it can be used for tasks such as classification or regression. The first layer of a neural network accepts the input signals, and the last layer for outputs. Here each node (unit) in the input or output layer corresponding

to one component of the inputs or outputs when these are treated as a vector; note for simplicity here we omit the nodes corresponding to the bias terms. Each node in the intermediate layers (called *hidden layers*) takes inputs from all the connecting nodes in the previous layer, then performs a nonlinear activation operation and outputs the resulting signals to those connecting nodes in the next layer. As the data flows from one layer to the next, a weight is applied at all the connecting links. An illustration of the deep neural network is given in Figure 5. In the following, we will formally describe the details.

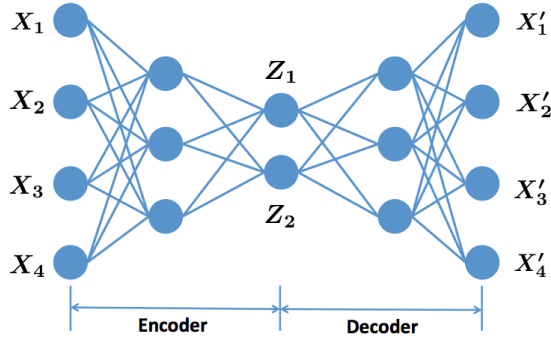


Figure 5: Illustration of deep neural network and autoencoder. X_1, \dots, X_4 are components of the inputs and Z_1, Z_2 are components of the codewords.

Assume the input data is represented by a matrix $\mathbf{X}_{N \times p}$, where N is the number of data instances and p is the data dimension or the number of nodes in the input layer. Let the weights to the links connecting the $(i-1)$ -th and i -th hidden layer be denoted by $\mathbf{W}^{(i)}$, with its dimension determined by the number of nodes involved. Let the output signal from the i -th hidden layer be denoted by $\mathbf{Z}^{(i)}$. Let σ be the nonlinear activation function (assume all hidden layers have the same activation function for simplicity). Assume there are K hidden layers. Then the output signals at the first hidden layer are given by

$$\mathbf{Z}^{(1)} = \sigma \left(\mathbf{W}^{(1)} \mathbf{X} + \mathbf{b}^{(1)} \right).$$

With the convention $\mathbf{Z}^{(0)} = \mathbf{X}$, the output signals at the i -th hidden layer can be expressed as

$$\mathbf{Z}^{(i)} = \sigma \left(\mathbf{W}^{(i)} \mathbf{Z}^{(i-1)} + \mathbf{b}^{(i)} \right), i = 1, 2, \dots, K.$$

Often the training of the neural network is formulated as solving

$$\arg \min_{\mathbf{W}, \mathbf{b}} J(\mathbf{W}, \mathbf{b}, \mathbf{X}, \mathbf{Y}) = l \left(\mathbf{Z}^{(K)}, \mathbf{Y} \right) - \frac{\lambda}{2} \cdot \|\mathbf{W}\|, \quad (1)$$

where $l(\cdot)$ is a loss function (e.g., squared error for regression or cross entropy for classification), and $\|\cdot\|$ is a norm such as the L_2 norm. The solution to (1) is often obtained by the *back-propagation* algorithm. $\mathbf{Z}^{(K)}$ is obtained from \mathbf{X} by the composition of a series of functions

$$\sigma \circ \mathbf{W}^{(K)} \dots \sigma \circ \mathbf{W}^{(2)} \sigma \circ \mathbf{W}^{(1)},$$

thus it can be written as $\mathbf{Z}^{(K)} = f_{\mathbf{W},b}(\mathbf{X})$ for some function $f_{\mathbf{W},b}$, which can be viewed as a smoothing function (or transformation) of the data. When the output \mathbf{Y} is the same as the input \mathbf{X} , the neural network is called an autoencoder. The deep network in Figure 5 becomes an autoencoder when all $X'_i = X_i$; Z_1, Z_2 are components of the codewords, that is, $(X_1, \dots, X_4) \rightarrow (Z_1, Z_2)$.

Although not necessary but typically an autoencoder can be divided as the encoder part and the decoder part which are mirror-symmetric (i.e., corresponding layers have the same number of units or connecting weights) w.r.t. the layer in the center. If some hidden layer has less units than that of the inputs, that means the data \mathbf{X} , at certain stage of its transformation, has a dimension less than the original dimension thus achieving a dimension reduction effect. For example, in Figure 5, the original data dimension is 4 and the transformed data has a dimension of 2. If one is willing to assume that the activation function is smooth, then the data can be viewed as lying on a low dimensional manifold. The fitting of the neural network can thus be viewed as a way of learning the low-dimensional manifold. As the activation is nonlinear, the resulting manifold is also nonlinear. As individual hidden layers in a neural network can be viewed as extracting features of the original data, we will use such features as representation of the low dimensional manifold. These features are called *M-features*, to be appended to the existing GLCM features in the scoring of TMA images.

Note that we state in Section 1 that for TMA images, the training sample size is often far less than that required by a typical deep neural network. However, we could still use the autoencoder, for two reasons. First the deep representation we will extract with an autoencoder is to be used for regularization, thus it would be sufficient as long as the representation captures main features of the manifolds. Second, we can control the size of the deep network according to the training sample size; indeed we will be using the simplest autoencoder, that is, with only one hidden layer in this work. The algorithm for manifolds extraction is simply to extract information of the trained hidden layer, when using some deep neural network package (The *deepnet* package is used in this work). Let *nHidden* be the dimension of the low-dimensional manifold. An algorithmic description is given as Algorithm 2.

Algorithm 2 *mfLearner*($\mathbf{X}, nHidden$)

- 1: $dnn \leftarrow dbn.dnn.train(\mathbf{X}, \mathbf{X}, nHidden)$;
 - 2: Extract from *dnn* a low-dimensional representation $\cup_{i=1}^N \{Z_i\}$;
 - 3: Return($\cup_{i=1}^N \{Z_i\}$);
-

3 Experiments

We conduct experiments on TMA images, the data at which our methods are primarily targeting. The TMA images are taken from the Stanford Tissue Microarray Database (<http://tma.stanford.edu/>, see [37]). TMAs corresponding to the biomarker, estrogen receptor (ER), for breast cancer tissues are used since ER is a known well-studied biomarker. There

are a total of 695 such TMA images in the database, and each image is scored at four levels (i.e., label), from $\{0, 1, 2, 3\}$.

The GLCM corresponding to $(\nearrow, 3)$ is used, which, according to [56], is the spatial relationship that leads to the greatest discriminating power for ER/breast cancer. The pathological interpretation is that, the staining pattern is approximately rotationally invariant (thus the choice of direction is no longer important) and ‘3’ is related to the size of the staining pattern for ER/breast cancer.

For autoencoder, we use the R package *deepnet*. Random Forests (RF) [7] is chosen as the classifier due to its superior performance compared to popular methods such as support vector machines (SVM) [15] and boosting [18], according to large scale simulation studies [10]. This is also true for the scoring ([56]; [55]) and the segmentation of TMA images [29]. This is likely due to the high dimensionality (2601 when using GLCM) and the remarkable feature selection as well as noise-resistance ability of RF, while SVM and boosting methods are typically prone to those.

For simplicity, the test set error rate is used as our performance metric. In all experiments, a random selection of half of the data are used for training and the rest for test, and results are averaged over 100 runs. We conduct two types of experiments. One is to use linear manifolds extracted by PCA. The other is to use nonlinear manifolds extracted by autoencoder.

3.1 Experiments with manifolds by PCA

We mention in Section 2 that one can extract linear manifolds with PCA. How effective are those linear manifolds in the scoring of TMA images? We distinguish between two cases. One is to use the leading principal components as sole features to be input the classifier, the other is to use the leading principal components as regularizing features appended to the GLCMs. The results are shown in Figure 6 where we produce the test set error rates when the number of leading principal components increases up to 100. It can be seen that the PCA features as regularizing features clearly outperform that using those as sole features with a performance gap close to about 6%.

3.2 Experiments with manifolds by autoencoder

For nonlinear manifolds with autoencoder, we conduct experiments on three different cases: 1) Use all the original image pixels as features along with M-features extracted from the space of the original images; 2) GLCM features along with M-features extracted from the space of the original images; 3) GLCM features along with M-features extracted from the space of GLCMs. We also tried using M-features extracted from the space of original images alone and that of GLCMs alone, but none gave satisfactory results. Table 1 shows results obtained in the three cases where the dimension of the low-dimensional manifold varies.

Using original images pixels as features along with manifolds features extracted from the space of original images does not lead to satisfactory results, while using GLCMs with manifolds features from the space of

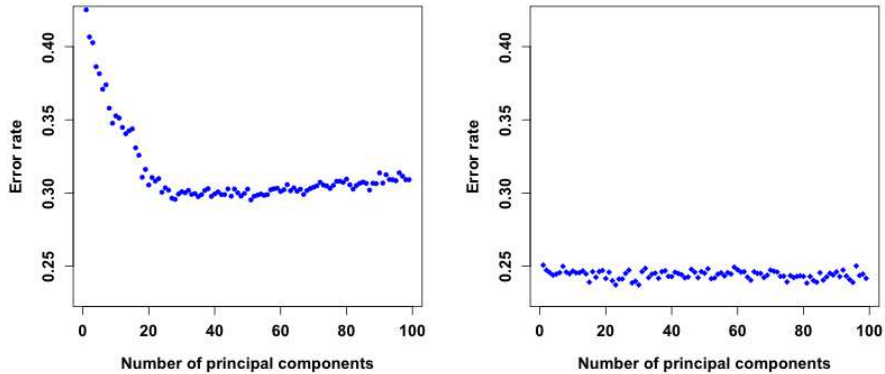


Figure 6: *Test set error rate when including more leading principal components. Left: using only principal components. Right: using both GLCM features and principal components.*

original images improves marginally over using GLCMs alone. The best result is achieved at an error rate of 22.85% when using GLCM features along with M-features extracted from the space of GLCMs with the dimension of the manifold being 25. Compared to an error rate of 23.28% achieved by *deepTacoma* [55] and 24.79% without using any deep features by *TACOMA* [56], the improvement is substantial given that the performance by *TACOMA* [56] already rivals pathologists, and that progress in this area is typically incremental in nature.

4 Conclusions

Inspired by the recent success of semi-supervised learning and deep learning, we explore deep representation learning under small data, in the context of TMA image scoring. In particular, we propose the *mfTacoma* algorithm to extract the low-dimensional manifolds in high dimensional data. Under *mfTacoma*, deep representations about the manifolds, possibly crude due to small data, are conveniently used as regularizing features to be appended to the original data features. This turns out to be a simple and effective way of making use of the low dimensional manifold information. Our experiments show that *mfTacoma* outperforms linear manifold features extracted by PCA or deep features of a group nature. We consider this a notable improvement over *TACOMA* and *deepTacoma* given that those already rival trained pathologists in the scoring of TMA images and progress in this area is typically incremental in nature.

Given the prevalence of low dimensional manifolds in high dimensional data, we expect that deep features derived from low dimensional manifolds would help in many applications. Our approach of leveraging the manifold information as regularizing features will be useful in small data setting, where one may incorporate feature weights by accounting for the sample size or data quality.

Features	Dim. of manifold	Error rate
GLCM	—	24.79%
Image + AE image features	100	29.89%
	50	29.88%
	25	29.90%
GLCM + AE image features	400	24.51%
	300	24.64%
	200	24.03%
	100	24.63%
	50	24.42%
	25	24.36%
	10	24.59%
GLCM + AE GLCM features	200	24.72%
	100	24.66%
	50	24.59%
	40	23.84%
	30	23.23%
	25	22.85%
	20	23.08%
	10	23.75%

Table 1: Error rate in scoring TMA images when using different deep features under different manifold dimensions. Note that the first row corresponds to results obtained by RF on the GLCM features alone (i.e., without deep features). Here ‘Image’ indicates when the original image pixels are used as features, ‘AE image features’ indicates manifold features extracted from the space of the original TMA images, ‘AE GLCM features’ indicates manifold features extracted from the space of the GLCM of the TMA images.

References

- [1] A. Beck, A. Sangoi, S. Leung, R. Marinelli, T. Nielsen TO, M. van de Vijver, R. West, M. van de Rijn, and D. Koller. Systematic analysis of breast cancer morphology uncovers stromal features associated with survival. *Science Translational Medicine*, 3(108):108–113, 2011.
- [2] M. Belkin and P. Niyogi. Laplacian eigenmaps for dimensionality reduction and data representation. *Neural Computation*, 15:1373–1396, 2003.
- [3] M. Belkin, P. Niyogi, and V. Sindhvani. Manifold regularization: A geometric framework for learning from labeled and unlabeled examples. *Journal of Machine Learning Research*, 7:2399–2434, 2006.
- [4] S. Bentzen, F. Buffa, and G. Wilson. Multiple biomarker tissue microarrays: bioinformatics and practical approaches. *Cancer and Metastasis Reviews*, 27(3):481–494, 2008.
- [5] A. Berger, D. Davis, C. Tellez, V. Prieto, J. Gershenwald, M. Johnson, D. Rimm, and M. Bar-Eli. Automated quantitative analysis of activator protein-2 α subcellular expression in melanoma tissue microarrays correlates with survival prediction. *Cancer research*, 65(23):11185, 2005.

- [6] P. J. Bickel and D. Yan. Sparsity and the possibility of inference. *Sankhya: The Indian Journal of Statistics, Series A (2008-)*, 70(1):1–24, 2008.
- [7] L. Breiman. Random Forests. *Machine Learning*, 45(1):5–32, 2001.
- [8] R. Camp, G. Chung, D. Rimm, et al. Automated subcellular localization and quantification of protein expression in tissue microarrays. *Nature medicine*, 8(11):1323–1327, 2002.
- [9] R. Camp, V. Neumeister, and D. Rimm. A decade of tissue microarrays: progress in the discovery and validation of cancer biomarkers. *Journal of Clinical Oncology*, 26(34):5630–5637, 2008.
- [10] R. Caruana, N. Karampatziakis, and A. Yessenalina. An empirical evaluation of supervised learning in high dimensions. In *Proceedings of the Twenty-Fifth International Conference on Machine Learning (ICML)*, pages 96–103, 2008.
- [11] B. J. Casey, F. Soliman, K. G. Bath, and C. E. Glatt. Imaging genetics and development: challenges and promises. *Human Brain Mapping*, 31(6):838–851, 2010.
- [12] L. Cayton. Algorithms for manifold learning. *Technical Report CS2008-0923, Department of Computer Science, UC San Diego*, 2008.
- [13] O. Chapelle, J. Weston, and B. Schölkopf. Cluster kernels for semi-supervised learning. In *Advances in Neural Information Processing Systems 15*, pages 601–608, 2003.
- [14] G. Chung, E. Kielhorn, and D. Rimm. Subjective differences in outcome are seen as a function of the immunohistochemical method used on a colorectal cancer tissue microarray. *Clinical Colorectal Cancer*, 1(4):237–242, 2002.
- [15] C. Cortes and V. N. Vapnik. Support-vector networks. *Machine Learning*, 20(3):273–297, 1995.
- [16] K. DiVito and R. Camp. Tissue microarrays—automated analysis and future directions. *Breast Cancer Online*, 8(7), 2005.
- [17] D. Donoho and C. Grimes. Hessian eigenmaps: Locally linear embedding techniques for high-dimensional data. *Proceedings of the National Academy of Sciences, U. S. A.*, 100(10):5591–5596, 2003.
- [18] Y. Freund and R. Schapire. Experiments with a new boosting algorithm. In *International Conference on Machine Learning (ICML)*, 1996.
- [19] G. Fromont, M. Roupret, N. Amira, M. Sibony, G. Vallancien, P. Validire, and O. Cussenot. Tissue microarray analysis of the prognostic value of E-Cadherin, Ki67, p53, p27, Survivin and MSH2 expression in upper urinary tract transitional cell Carcinoma. *European Urology*, 48(5):764–770, 2005.
- [20] J. Giltneane and D. Rimm. Technology insight: identification of biomarkers with tissue microarray technology. *Nature Clinical Practice Oncology*, 1(2):104–111, 2004.
- [21] P. Gong, D. Marceau, and P. J. Howarth. A comparison of spatial feature extraction algorithms for land-use classification with SPOT HRV data. *Remote Sensing of Environment*, 40:137–151, 1992.

- [22] I. Goodfellow, Y. Bengio, and A. Courville. *Deep Learning*. The MIT Press, 2016.
- [23] R. M. Gray and D. L. Neuhoff. Quantization. *IEEE Transactions of Information Theory*, 44(6):2325–2383, 1998.
- [24] R. M. Haralick. Statistical and structural approaches to texture. *Proceedings of IEEE*, 67(5):786–803, 1979.
- [25] S. Hassan, C. Ferrario, A. Mamo, and M. Basik. Tissue microarrays: emerging standard for biomarker validation. *Current Opinion in Biotechnology*, 19(1):19–25, 2008.
- [26] C. Hegde, M. Wakin, and R. Baraniuk. Random projections for manifold learning. In *Neural Information Processing Systems (NIPS)*, volume 20, 2007.
- [27] D. Hibar, O. Kohannim, J. Stein, M.-C. Chiang, and P. Thompson. Multilocus genetic analysis of brain images. *Frontiers in Genetics*, 2(73):1–11, 2011.
- [28] G. Hinton and R. Salakhutdinov. Reducing the dimensionality of data with neural networks. *Science*, 313:504–507, 2006.
- [29] S. Holmes, A. Kapelner, and P. Lee. An interactive Java statistical image segmentation system: Gemident. *Journal of Statistical Software*, 30(10):1–20, 2009.
- [30] H. Hotelling. Analysis of a complex of statistical variables into principal components. *Journal of Educational Psychology*, 24:417–441, 1933.
- [31] C. Hsu, D. Ho, C. Yang, C. Lai, I. Yu, and H. Chiang. Interobserver reproducibility of Her-2/neu protein overexpression in invasive breast carcinoma using the DAKO HercepTest. *American journal of clinical pathology*, 118(5):693–698, 2002.
- [32] X. Huo, X. Ni, and A. Smith. A survey of manifold-based learning methods. *Recent Advances in Data Mining of Enterprise Data*, pages 691–745, 2007.
- [33] J. Kononen, L. Bubendorf, A. Kallionimeni, M. Bärklund, P. Schraml, S. Leighton, J. Torhorst, M. Mihatsch, G. Sauter, and O. Kallioniemi. Tissue microarrays for high-throughput molecular profiling of tumor specimens. *Nature Medicine*, 4(7):844–847, 1998.
- [34] Y. LeCun, Y. Bengio, and G. Hinton. Deep learning. *Nature*, 521:436–444, 2015.
- [35] N. Lei, Z. Luo, S.-T. Yau, and D. X. Gu. Geometric understanding of deep learning. *arXiv:1805.10451*, 2018.
- [36] C. D. Lloyd, S. Berberoglu, P. J. Curran, and P. M. Atkinson. A comparison of texture measures for the per-field classification of Mediterranean land cover. *International Journal of Remote Sensing*, 25(19):3943–3965, 2004.
- [37] R. Marinelli, K. Montgomery, C. Liu, N. Shah, W. Prapong, M. Nitzberg, Z. Zachariah, G. Sherlock, Y. Natkunam, R. West, et al. The Stanford tissue microarray database. *Nucleic Acids Research*, 36:D871–877, 2007.
- [38] S. Mousses, L. Bubendorf, U. Wagner, G. Hostetter, J. Kononen, R. Cornelison, N. Goldberger, A. Elkhoulou, N. Willi, P. Koivisto,

- W. Ferhle, M. Raffeld, G. Sauter, and O. Kallioniemi. Clinical validation of candidate genes associated with prostate cancer progression in the cwr22 model system using tissue microarrays. *Cancer Research*, 62(5):1256–1260, 2002.
- [39] B. Nadler, S. Lafon, R. Coifman, and I. G. Kevrekidis. Diffusion maps - a probabilistic interpretation for spectral embedding and clustering algorithms. *Principal Manifolds for Data Visualization and Dimension Reduction (Lecture Notes in Computational Science and Engineering)*, 58:238–260, 2007.
- [40] S. Osher, Z. Shi, and W. Zhu. Low dimensional manifold model for image processing. *SIAM Journal on Imaging Sciences*, 10(4):1669–1690, 2017.
- [41] D. Perraul-Joncas and M. Meila. Non-linear dimensionality reduction: Riemannian metric estimation and the problem of geometric discovery. *arXiv:1305.7255*, 2013.
- [42] R. Pless and R. Souvenir. A survey of manifold learning for images. *IPSP Transactions on Computer Vision and Applications*, pages 83–94, 2009.
- [43] S. Roweis and L. Saul. Nonlinear dimensionality reduction by locally linear embedding. *Science*, 290(5500):2323–2326, 2000.
- [44] J. Schmidt-Hieber. Nonparametric regression using deep neural networks with ReLU activation function. *arXiv:1708.06633*, 2017.
- [45] C. Shahabi and D. Yan. Real-time pattern isolation and recognition over immersive sensor data streams. In *Proceedings of the 9th International conference on multi-media modeling*, pages 93–113, 2003.
- [46] J. Shlens. A tutorial on principal component analysis. *arXiv:1404.1100*, 2014.
- [47] J. B. Tenenbaum, V. de Silva, and J. C. Langford. A global geometric framework for nonlinear dimensionality reduction. *Science*, 290(5500):2319–2323, 2000.
- [48] T. Thomson, M. Hayes, J. Spinelli, E. Hilland, C. Sawrenko, D. Phillips, B. Dupuis, and R. Parker. HER-2/neu in breast cancer: interobserver variability and performance of immunohistochemistry with 4 antibodies compared with fluorescent in situ hybridization. *Modern Pathology*, 14(11):1079–1086, 2001.
- [49] US National Cancer Institute. <https://www.cancer.gov/about-cancer/understanding/what-is-cancer>.
- [50] D. Voduc, C. Kenney, and T. Nielsen. Tissue microarrays in clinical oncology. *Seminars in radiation oncology*, 18(2):89–97, 2008.
- [51] H. Vrolijk, W. Sloos, W. Mesker, P. Franken, R. Fodde, H. Morreau, and H. Tanke. Automated Acquisition of Stained Tissue Microarrays for High-Throughput Evaluation of Molecular Targets. *Journal of Molecular Diagnostics*, 5(3):160–167, 2003.
- [52] R. Walker. Quantification of immunohistochemistry - issues concerning methods, utility and semiquantitative assessment I. *Histopathology*, 49(4):406–410, 2006.
- [53] W. H. Wan, M. B. Fortuna, and P. Furmanski. A rapid and efficient method for testing immunohistochemical reactivity of monoclonal antibodies against multiple tissue samples simultaneously. *Journal of Immunological Methods*, 103:121–129, 1987.

- [54] D. Yan, P. Bickel, and P. Gong. A bottom-up approach for texture modeling with application to Ikonos image classification. *Submitted*, 2018.
- [55] D. Yan, T. W. Randolph, J. Zou, and P. Gong. Incorporating deep features in the analysis of tissue microarray images. *Statistics and Its Interface*, 12(2):283–293, 2019.
- [56] D. Yan, P. Wang, B. S. Knudsen, M. Linden, and T. W. Randolph. Statistical methods for tissue microarray images—algorithmic scoring and co-training. *The Annals of Applied Statistics*, 6(3):1280–1305, 2012.
- [57] Z. Zhang and H. Zha. Principal manifolds and nonlinear dimension reduction via local tangent space alignment. *SIAM Journal on Scientific Computing*, 26(1):313–338, 2004.
- [58] H. Zhao, P. C. Yuen, and J. T. Kwok. A novel incremental principal component analysis and its application for face recognition. *IEEE Transactions on Systems, Man, and Cybernetics—Part B: Cybernetics*, 36(4):873–886, 2006.
- [59] X. Zhu. Semi-supervised learning literature survey. *TR 1530, Department of Computer Science, University of Wisconsin-Madison*, 2008.